Predictions on Heat Transport and Plasma Rotation from Global Gyrokinetic Simulations

Y Sarazin[1], **V Grandgirard**[1], **J Abiteboul**[1], **S Allfrey**[1], **X Garbet**[1], **Ph Ghendrih**[1], **G Latu**[1], **A Strugarek**[1], **G Dif-Pradalier**[2], **P H Diamond**[2,3], **S Ku**[4], **C S Chang**[4], **B F McMillan**[5], **T M Tran**[5], **L Villard**[5], **S Jolliet**[6], **A Bottino**[7], **P Angelino**[8]

[1] CEA, IRFM, F-13108 Saint-Paul-lez-Durance, France.
[2] Center for Astrophysics and Space Sciences, UCSD, La Jolla, California 92093, USA.
[3] National Fusion Research Institute, Daejeon, Republic of Korea.
[4] Courant Institute of Mathematical Sciences, New York Univ., New York 10012, USA.
[5] Centre de Recherches en Physique des Plasmas, Association Euratom-Confédération Suisse, Ecole Polytechnique Fédérale de Lausanne, 1015 Lausanne, Switzerland.
[6] Japan Atomic Energy Agency, Higashi-Ueno 6-9-3, Tokyo 110-0015, Japan.
[7] Max-Planck Institut für Plasmaphysik, Association Euratom, Garching, Germany.
[8] Laboratory of Computational Systems Biotechnology, EPFL, 1015 Lausanne, Switzerland.

E-mail: `yanick.sarazin@cea.fr`

Abstract.
Flux-driven global gyrokinetic codes are now mature enough to make predictions in terms of turbulence and transport in tokamak plasmas. Some of the recent breakthroughs of three such codes, namely GYSELA, ORB5 and XGC1, are reported and compared wherever appropriate. In all three codes, turbulent transport appears to be mediated by avalanche-like events, for a broad range of $\rho_* = \rho_i/a$ values, ratio of the gyro-radius over the minor radius. Still, the radial correlation length scales with ρ_i, leading to the gyroBohm scaling of the effective transport coefficient below $\rho_* \approx 1/300$. The possible explanation could be due to the fact that avalanches remain meso-scale due to the interaction with zonal flows, whose characteristic radial wave-length appears to be almost independent of the system size. As a result of the radial corrugation of the turbulence driven zonal and mean flows, the shear of the radial electric field can be significantly underestimated if poloidal rotation is assumed to be governed by the neoclassical theory, , especially at low collisionality. Indeed, the turbulence contribution to the poloidal rotation increases when collisionality decreases. Finally, the numerical verification of toroidal momentum balance shows that both neoclassical and turbulent contributions to the Reynolds' stress tensor play the dominant role. The phase space analysis further reveals that barely passing supra-thermal particles mostly contribute to the toroidal flow generation, consistently with quasi-linear predictions.

1. Introduction

Predicting the performance of fusion plasmas in terms of quality factor, the ratio of fusion power to injected power, is among the key challenges in fusion plasma physics. To achieve this goal, turbulence and heat transport needs to be modeled within the most accurate theoretical framework, using state-of-the-art non-linear simulation tools. The gyrokinetic equation for each species, coupled to Maxwell's equations, constitutes our best self-consistent description of this problem. One of the key modeling issues is the type of forcing that should be applied to the system. In order to approach experimental conditions, new types of code have recently emerged, in which turbulence is driven by some prescribed external heat or momentum source [1].

The most recent results obtained with three such codes, namely GYSELA [2], ORB5 [3] and XGC1 [4], are discussed in a coherent perspective. The focus is put on predictions of heat turbulent transport and plasma rotation in tokamaks. Much material comes from GYSELA simulations, but common features with respect to the two other codes are highlighted whenever appropriate. Section 2 details the models, with special emphasis on the main differences between the codes, in particular regarding the source term. In section 3, the turbulent transport dynamics is shown to exhibit large scale avalanche-like events, which propagate in both directions (inward and outward) at about the diamagnetic drift velocity. The scaling law of the effective heat diffusivity with respect to the normalized gyro-radius ρ_* shows a departure from the gyro-Bohm scaling below $\rho_* \approx 1/300$. Attempts to trigger transport barriers are also reported. Finally, section 4 addresses plasma rotation issues, both poloidal and toroidal. Two main results are obtained. First, the $\mathbf{E} \times \mathbf{B}$ shearing rate can be significantly (by factors) underestimated when computed from the radial force balance equation, if the poloidal rotation is assumed to be governed by the neoclassical theory only, excluding the turbulence contribution. Secondly, the turbulence generation of toroidal rotation is found to originate from barely passing supra-thermal particles, in agreement with quasi-linear predictions.

2. Main characteristics of GYSELA, XGC1 and ORB5 codes

The non-linear results of three gyrokinetic codes GYSELA [2], ORB5 [3] and XGC1 [4] are analyzed and compared. Although they use different numerical schemes, all three share the essential characteristics necessary to capture the rich dynamics of flux-driven turbulent transport. Firstly, they are global: a large fraction of the plasma radius is considered. This is in contrast to flux-tube codes which focus on the small volume around magnetic field lines by proceeding from a scale separation assumption, the fluctuation scale length being smaller than that of the equilibrium. In such codes, periodicity is assumed along the radial direction. Conversely, global codes face the delicate problem of radial boundary conditions. Basically, non-axisymmetric fluctuations of the electric potential and of the distribution function – i.e. $(m, n) \neq (0, 0)$ modes, with m and n the poloidal and toroidal wave numbers – are forced to zero at both radial boundaries of the simulated domain, except for ORB5 which resolves the magnetic axis. As far as the axisymmetric component is concerned, the value of the potential is prescribed at the outer boundary, while the radial electric field is set to zero at the inner boundary (except for ORB5 in which only unicity of the potential is prescribed). Secondly and very importantly, these codes are full-f, such that the back

reaction of turbulent transport is accounted for in the time evolution of the equilibrium. Notice that, although ORB5 uses the splitting $f = \delta f + f_0$ to improve numerical performance, the full-f equations are implemented, without any assumption on the relative size of f_0 and δf [5]. In such cases, the turbulence regime is evanescent if no free energy is injected in the system. Indeed, turbulent transport results in the flattening of the temperature profile, which would ultimately reach marginal stability in the absence of any forcing. In this framework, a heat source is mandatory in view of exploring the long time – on energy confinement times – behavior of turbulence and transport. To our knowledge, the first attempt to investigate flux-driven turbulent transport in kinetic models for fusion magnetized plasmas was undertaken in a reduced model for trapped ion mode turbulence [6]. Let us finally remark that even local gyro-kinetic codes are in the process of incorporating global effects, by taking into account the mean profile relaxation, although in a less consistent way than global codes [7, 8].

The simulations focus on electrostatic Ion Temperature Gradient (ITG) driven turbulence with adiabatic electrons. The set of equations solved is derived from the modern formulation of gyro-kinetic theory [9]. We detail the formulation adopted in the GYSELA code, and outline the main differences with respect to the two other codes, ORB5 and XGC1. The equations for the entire ion guiding-center distribution function $f(r, \theta, \varphi, v_{G\parallel}, \mu, t)$:

$$B_\parallel^* \partial_t f + \boldsymbol{\nabla} \cdot \left(B_\parallel^* \, \dot{\mathbf{x}}_G \, f \right) + \partial_{v_{G\parallel}} \left(B_\parallel^* \, \dot{v}_{G\parallel} \, f \right) = \mathcal{C}(f) + S \qquad (1)$$

$$B_\parallel^* \, \dot{\mathbf{x}}_G = v_{G\parallel} \mathbf{B}^* + \mathbf{b} \times \boldsymbol{\nabla}\Xi/e \quad ; \qquad B_\parallel^* \, \dot{v}_{G\parallel} = -\mathbf{B}^* \cdot \boldsymbol{\nabla}\Xi/m_i \qquad (2)$$

with $\boldsymbol{\nabla}\Xi = \mu\boldsymbol{\nabla}B + e\boldsymbol{\nabla}\bar{\phi}$ and $\mathbf{B}^* = \mathbf{B} + (m_i/e)\, v_{G\parallel}\boldsymbol{\nabla} \times \mathbf{b}$. The collision operator $\mathcal{C}(f)$ and the source term S are detailed below. $\bar{\phi}$ is the gyro-averaged electric potential. The scalar $B_\parallel^*$ is $B_\parallel^* = \mathbf{B}^* \cdot \mathbf{b}$, with $\mathbf{b} = \mathbf{B}/B$. Electrons are assumed adiabatic, with the implication that particle transport vanishes. The system is closed by the quasi-neutrality condition:

$$\frac{e}{T_{e,eq}} \, (\phi - \langle\phi\rangle) - \frac{1}{n_{eq}} \, \boldsymbol{\nabla}_\perp \cdot \left(\frac{m_i n_{eq}}{eB^2}\boldsymbol{\nabla}_\perp\phi \right) = \frac{n_G - n_{G,eq}}{n_{eq}} \qquad (3)$$

with $\boldsymbol{\nabla}_\perp = (\partial_r, \frac{1}{r}\partial_\theta)$ and $\nabla_\parallel = \frac{1}{R}(\partial_\varphi + \frac{1}{q}\partial_\theta)$. Here, φ is the toroidal angle and θ the straight-field-line poloidal coordinate. The polarisation density (second term on the left hand side of Eq. 3) is approximate, valid only in the limit of long wavelengths $k_\perp\rho_i \ll 1$. The guiding-center density is defined by: $n_G = \iint \mathcal{J}_v \, \mathrm{d}\mu \, \mathrm{d}v_{G\parallel}(J.f)$, with J the gyro-average operator and $\mathcal{J}_v = 2\pi B_\parallel^*/m_i$ the Jacobian in the velocity space. f is replaced by the equilibrium component f_{eq} when computing n_{eq}. $\langle\phi\rangle$ stands for the flux surface average of the electric potential, defined by $\langle\phi\rangle = \iint \mathcal{J}_x \, \phi \, \mathrm{d}\theta \, \mathrm{d}\varphi / \iint \mathcal{J}_x \, \mathrm{d}\theta \, \mathrm{d}\varphi$, with $\mathcal{J}_x = (\mathbf{B} \cdot \boldsymbol{\nabla}\theta)^{-1}$ the configuration space Jacobian. The initial state consists in an equilibrium Maxwellian distribution function, which is either local or canonical (both choices are relevant at finite collisionality), plus a bath of poloidal and toroidal modes of small amplitude.

Both ORB5 and XGC1 are Particle In Cell (PIC) codes, while GYSELA uses the backward-in-time semi-Lagrangian scheme [10]. They have been successfully benchmarked against several linear predictions, namely growth rates and real frequencies of the most unstable modes in the unstable ITG regime, and the oscillatory decay towards residual poloidal flow in the collisionless regime, according to Rosenbluth-Hinton

prediction [11]. In XGC1 and ORB5, Coulomb collisions are modeled by a linearized Monte Carlo scheme [12, 13, 14, 15, 16], while a Fokker-Planck operator acting on $v_{G\parallel}$ only is used in GYSELA [17, 18, 19]. Both collision schemes conserve particles, momentum and energy, and the full distribution function relaxes towards the isotropic Maxwellian, according to the H-theorem (Boltzmann). Also, the schemes have been shown to reproduce neoclassical physics [14, 18, 19, 20]. While GYSELA employs a simplified magnetic equilibrium with circular, concentric magnetic flux surfaces, both ORB5 and XGC1 are capable of handling more realistic geometries. Importantly, XGC1 may model an X-point at the plasma periphery. In addition, two of these codes, namely GYSELA and ORB5, participated to the successful effort of nonlinear benchmark in the gradient-driven regime of several European codes within the EFDA Task Force on Integrated Tokamak Modeling [21].

The source term aims at maintaining the equilibrium profiles, which would otherwise relax towards marginal state. Different expressions have been used in the three codes. In GYSELA, the source consists of the sum of the product of Hermite and Laguerre polynomials in $v_{G\parallel}$ and μ, respectively, in the spirit of the pioneering work by Darmet *et al.* [6]. It is versatile enough to allow for separate injection of heat, parallel momentum and vorticity. Such a versatility imposes serious constraints on the expression of the source in phase space, as detailed in Appendix A. The separation between these three kinds of sources is achieved by using projections onto the bases of orthogonal polynomials in $v_{G\parallel}$ and μ, namely Hermite and Laguerre polynomials. The retained expression for the heat source directly derives from such constraints. Especially, it is anisotropic in velocity space, such that parallel energy only is injected into the system. Indeed, up to small terms detailed in the appendix, the heat source term reads as follows:

$$S_{GYSELA} \simeq S_r \left[\left(\frac{v_{G\parallel}}{v_{Ts}} \right)^2 - 1 \right] \exp \left(-\frac{m_i v_{G\parallel}{}^2/2 + \mu B_0}{T_s} \right) \qquad (4)$$

with v_{Ts} an arbitrary normalizing velocity. The prescribed radial profile S_r is the sum of two hyperbolic tangents, and is localized close to the inner boundary of the simulation domain [22]. Redistribution of the energy towards transverse velocity space takes place on collisional time scales only. Indeed, the collision operator forces the system to relax towards the Maxwellian distribution function, calculated from the instantaneous and local parallel flow and the isotropic temperature T: no distinction is made between $T_\parallel$ and $T_\perp$, such that $T = T_\parallel + T_\perp$.

As far as XGC1 is concerned, heating is achieved by increasing the particle energy close to the inner radial boundary at uniform rate, while keeping the particle pitch angle fixed [4]. Such a technique looks like the particle-in-cell isotropic analogue to the one used in GYSELA. Indeed, S_{GYSELA} also proceeds by transferring particles from the sub-thermal to the supra-thermal domain, as evident from eq.4. In addition, an artificially large collisionality is prescribed in this region only in XGC1 so that the system smoothly transfers this energy to the turbulent region. In this case, both the spatial locality and the time independence of the heat source S_{XGC1} are ensured, similarly to the choice adopted in GYSELA.

In ORB5, the source term applies to the time evolution of δf. It is given in the form of the following Krook operator [23]:

$$S_{ORB5} = -\gamma_H \left(\delta f_{|v_{G\parallel}|} - f_{eq} \frac{\int \mathrm{d}^3\mathbf{v}\, \delta f_{|v_{G\parallel}|}}{\int \mathrm{d}^3\mathbf{v}\, f_{eq}} \right) \qquad (5)$$

Here, $\delta f_{|v_{G\parallel}|}$ stands for the expression of δf which is symmetrized in $v_{G\parallel}$, in order for the source to conserve parallel momentum. Such a time dependent heat source damps the components of the perturbed distribution δf on a time scale γ_H^{-1}, while only leading to a mild reduction of zonal flows in the collisionless linear regime. This results in a limited relaxation of the equilibrium gradient. One can identify two main differences with respect to the kind of source used in GYSELA. Firstly, S_{ORB5} is not constant in time since it depends on the actual distribution function. As a result, the amount of injected power evolves in time, in a way which can not be predicted *a priori*: it increases with heat turbulent transport. Secondly, it is not localized in space: it applies wherever the actual local distribution function departs from f_{eq}. In the end, the amount of heat power in ORB5 is proportional to $\nu\,\delta p(r,t)$, where the local pressure deviation is $\delta p(r,t) = n(r)\,[T(r,t) - T(r,0)]$. In the simulations reported here, the constant injection rate is $\nu = 3.5\,10^{-3}c_s/a$.

There are two main advantages of dealing with a prescribed heat source: (*i*) the forcing of turbulence mimics that in experiments, contrary to simulations where the mean gradient is prescribed, and (*ii*) the sum of the spatially and time (on the τ_E time scale) averaged turbulent and neoclassical heat fluxes is forced to equal the prescribed driving flux. In this case, the response is the temperature gradient, which ultimately governs the internal energy and therefore the performance of the discharge. Flux driven simulations then allow for investigating the impact of heating power on energy confinement time. Such an analysis is time consuming, and requires more CPU time at small ρ_*. For this reason, a relatively large ρ_* (1/64) was used. Degradation of confinement was observed when increasing the injected heating power P_{add} with GYSELA, with the scaling exponent $\tau_E \sim P_{add}^{-0.76\pm0.04}$, the same order of magnitude as that reported in the ITER database of L-mode plasmas [22]. In the simulations, such a behavior was reported to be correlated with the modification of the frequency spectrum of the turbulent heat flux at larger heat source. More precisely, the left and right cut-offs of the 1/f part of the frequency spectrum (with f the Fourier frequency) extend towards smaller and larger frequencies, respectively: both high and small frequency avalanches (see next section) exhibit larger magnitude. Interestingly, such a balanced modification does not appear to impact the skewed probability density function of the radial heat flux, which remains almost unchanged when the heat source magnitude is varied.

3. Transport dynamics and scaling properties

A general feature of flux-driven turbulence simulations, which is already well documented in fluid simulations [24, 25], is that turbulent transport exhibits avalanche-like events, characterized by large scale intermittent outbursts. These bursts, which are easily identified on flux surface averaged maps of the heat flux (cf. Fig. 1), propagate almost ballistically on large radial scales, much larger than the Eulerian correlation length of turbulence. These avalanches lead to an asymmetric probability density function of the turbulent flux, which is skewed towards large scale events. The avalanches significantly contribute to the local radial flux, as exemplified on Fig. 2 (obtained from GYSELA data of Fig. 1a). For instance, it appears that the largest scale events, representing a fraction of about 35% of the total events, can carry up to almost 48% of the local turbulent heat flux. Avalanches are found to all the
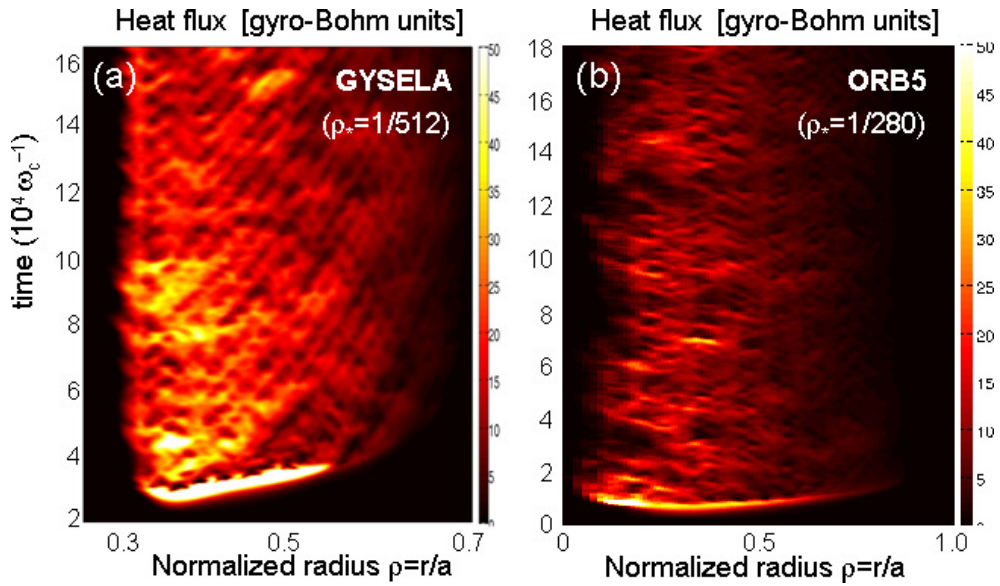
Figure 1. Color plots of the turbulent heat flux in the two-dimensional space (r,t) for two global gyrokinetic codes, namely GYSELA (a) and ORB5 (b). The same color scale has been adopted, which results in lesser contrast on the ORB5 plot.
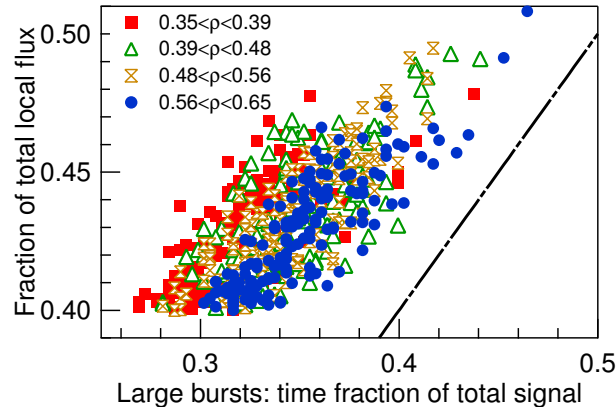

Figure 2. Fraction of the local radial turbulent heat flux carried out by a certain fraction of the largest scale bursts, as estimated from Fig. 1a (GYSELA data). Each point refers to one specific radial location. The colors allow one to distinguish four different radial domains. The considered time series ranges from $\omega_{c0}t = 56\,000$ to $\omega_{c0}t = 163\,000$.

more contribute to the local flux since they are close to the source region, at small normalized radii ρ. Indeed, on average, blue dots ($0.56 < \rho < 0.65$) are closer to the first diagonal than red squares ($0.35 < \rho < 0.39$). In the saturated turbulent regime, their propagation velocity is a fraction of the diamagnetic velocity $v_i^* \approx \rho_* v_T$, with $\rho_* = \rho_i/a$ the gyroradius normalised to the minor radius a, and v_T the ion thermal velocity. They are predicted to reach velocities of a few kilometers per second in ITER. These large scale events are clearly visible on Fig. 1 and Fig. 3. Interestingly enough, the first relaxation event which immediately follows the turbulence overshoot, after the exponential growth of the linear phase, propagates radially at a much higher speed than v_i^* in both codes. One possible reason for such a difference between the first and the other avalanches resides in the existence of wake effects for the latter ones: the first avalanche propagates into a turbulence free region, while the others face the already established turbulent eddies of the electric potential, which partly result from the previous avalanches. The $\rho_* = 1/512$ simulation with GYSELA, Fig. 1a, required about 275 billion grid points ($N_r \times N_\theta \times N_\varphi \times N_{v_{G\|}} \times N_\mu = 1024 \times 1024 \times 128 \times 128 \times 16$ for quarter of a torus), and ran about one month on 8192 processors. The ρ_* value corresponds to the one at mid-radius $r/a = 0.5$. Simulations with different ρ_* values are obtained by changing the minor radius a, all other parameters being kept fixed, including the aspect ratio R/a.
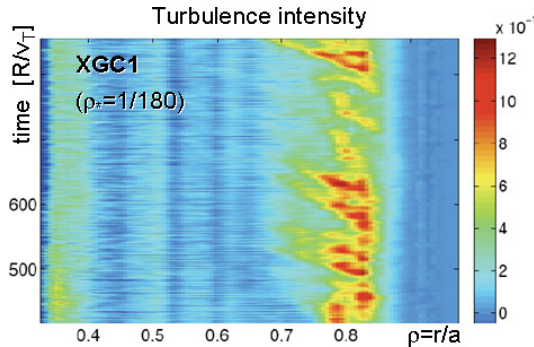

Figure 3. Color plot of the turbulence intensity in the two-dimensional space (r,t) for XGC1.

Notice that, when turbulence is primarily excited in the edge plasma region, as in XGC1 simulations with an initially large temperature gradient close to the last closed flux surface [14], fronts of temperature then propagate inwards, at the same speed as outgoing avalanches. Such a simulation does not last long enough for the large initial equilibrium temperature gradient to be significantly eroded. In addition, the core energy source S_{XGC1} is adjusted to prevent any strong evolution of the core temperature profile. Although we do not claim here that these phenomena are necessarily similar in essence, we remark that this impact of edge turbulence on core transport via long range ballistic inward bursts echoes some of the experimental observations in H-mode plasmas. Indeed, in this case, it was reported on JET that large type I ELMs (Edge Localized Modes) generate strong negative temperature perturbations that propagate inward on ballistic time scales [26]. These events can even erode, and ultimately destroy, internal transport barriers, likely making ITBs and H-mode type I ELM plasmas incompatible. The whole sequence observed in XGC1 appears to mimic

this post-relaxation phase, characterized by the inner penetration of the ELM-induced perturbation. Obviously, in XGC1, the perturbation does not originate from ELM relaxations, but from large bursts of turbulence intensity.

Such intermittent and ballistic dynamics are associated with local profile relaxations, and can produce a "sand pile effect". The essential feature governing such events is therefore the back reaction of turbulent transport on the equilibrium profile. As such, flux-driven simulations are not mandatory to observe avalanches *a priori*. Conversely, the scale separation assumption between equilibrium and fluctuations conflicts with this type of dynamics. For intermediate ρ_* values at least ($\rho_* = 1/64$), avalanches are found to correlate with streamer-like structures of the convection cells, albeit that their Fourier spectrum departs significantly from that of the most unstable linear modes [22]. For sufficiently small ρ_* (typically $< 1/256$), the shearing regions generated by the self-generated zonal flows appear to control the radial extent of the avalanches – although the converse cannot be excluded *a priori*, namely that the avalanche mean size governs the position of zonal flows [27]. Besides, the direction of propagation of the avalanches depends on the sign of the local shearing rate [28, 29]: radial regions with positive (resp. negative) shearing rates are associated with outward (resp. inward) events. Such ingredients are revealed to be extremely powerful when deriving reduced transport models to capture the essence of avalanche-like transport [28, 27]. One important feature of zonal flow radial structures is that they exhibit a characteristic wave-like shape. This is particularly clear on Fig. 4, where the instantaneous profiles (during the saturated non linear regime) of the poloidal component of the electric drift $\langle v_{E\theta} \rangle$ are displayed for two simulations with different ρ_* values. Here, the radial coordinate is normalized to the ion Larmor radius at mid-radius ($r/a = 0.5$), denoted ρ_0. Also, the thermal velocity at mid-radius is denoted v_{T0}. As already noted, such a shape is reminiscent of the negative viscosity nature of the Reynolds stress tensor [30]. Also, consistently with the "staircase" picture [27], their characteristic radial spacing does not scale with the system size a. Conversely, it saturates at intermediate meso-scales – well above the local-like turbulence autocorrelation length. As such, it emphasizes the central role for self-organization at these intermediate meso-scales and the turbulence-induced mean profile dynamics [31]. Two distinct dynamical regimes of zonal flows are actually observed in the simulations: they can either exhibit an almost vanishing frequency, such that their radial location does not much evolve in time (see e.g. [32, 27]), or the radial oscillations of $\langle v_{E\theta} \rangle$ can exhibit similar space-time dynamics as the one of the turbulent heat flux reported on Fig. 1a. This latter case prevails in the simulations of GYSELA reported in this paper. The main control parameter of this transition seems to be the departure from the stability threshold, zero-frequency zonal flows being preferentially observed close to the threshold. An ongoing work intends to clarify this preliminary observation. Also, it should be noted that, in most simulations including the ones reported here, $\langle v_{E\theta} \rangle$ exhibits time oscillations at the GAM (Geodesic Acoustic mode) frequency, $\omega_{GAM} \sim c_s/R$, at the very beginning of the non linear phase only. Then, these modes are rapidly damped out by both collisions and wave-particle resonances (Landau damping).

The scaling properties, especially with respect to ρ_*, of avalanche-dominated turbulent transport is a matter of concern for predicting the performance of next step devices, including ITER. First because ρ_* strongly impacts the energy confinement time, $\omega_c \tau_E \sim \rho_*^{-2.83}$ according to ITER scaling law for ELMy H-modes ($\omega_c \tau_E \sim \rho_*^{-1.85}$
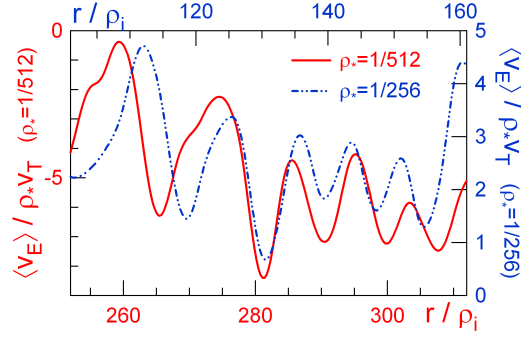
Figure 4. Radial profile of the flux surface averaged poloidal component of the $\mathbf{E} \times \mathbf{B}$ drift for two values of ρ_* (GYSELA runs). The wave-like structure of the zonal flows is almost independent of the system size a, since both curves exhibit similar characteristic wave length when expressed in ρ_i units.
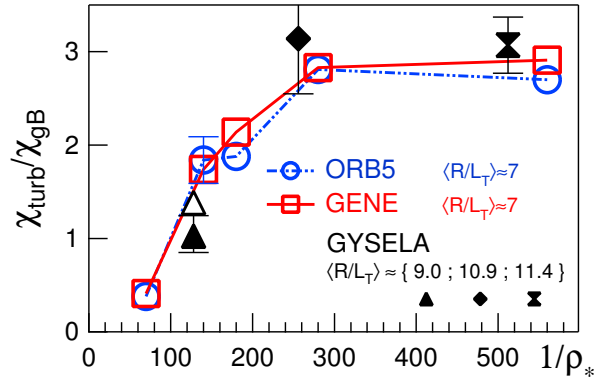

Figure 5. Effective heat diffusivity of three global gyrokinetic codes as function of ρ_* (the figure without the points of GYSELA is adapted from [34]).

in L-mode) [33]. Second because avalanches could break the gyro-Bohm scaling of turbulence, due to their large radial excursion over a significant portion of the system size. Scanning ρ_* from $1/70$ to $1/560$ with ORB5 reveals that the effective heat diffusion coefficient exhibits a deviation from the infinite system size limit gyro-Bohm scaling, with a value extrapolated to $\rho_* \to 0$ of $\chi/\chi_{\mathrm{gB}} \approx 3.2$ for Cyclone base case parameters [34]. The same results are obtained with the global version of the Eulerian GENE code [35], while the local version's predictions appear consistent with $\rho_* = 1/560$ simulations. A similar scan has been undertaken with GYSELA. Three points from GYSELA are overlaid on top of those from ORB5 and global GENE, Fig. 5. The GYSELA simulations devoted to the ρ_* scaling were not dedicated to this comparison. As a result, the main parameters depart from the Cyclone base case used in ORB5 and GENE simulations. Especially, the q-profile is given by $q(r) = q_0 + \delta_q (r/a)^{\alpha_q}$, with $q_0 = 1$, $\delta_q = 2.78$ and $\alpha_q = 2.8$ (the magnetic shear is equal to $s = 0.8$ at mid-radius), the aspect ratio is $R/a = 3.2$, and collisions are taken into account ($\nu_* = 0.1$). Also, the mean temperature gradient departs from

the one used in ORB5 and global GENE simulations. These differences would make dubious any quantitative comparison of the absolute magnitudes of the transport coefficients. Conversely, comparing the dependency with respect to ρ_* remains fully relevant, since, to our knowledge, no dependence on other parameters but ρ_* of the transition value between Bohm and gyro-Bohm scalings has been reported so far, neither experimentally nor theoretically. The vertical bars refer to the fluctuations of the effective turbulent diffusivity in the time window considered for the average (in the saturated turbulent regime). In order to account for the known dependency of the effective transport diffusivity with respect to R/L_T [36], the open triangle at $\rho_* = 1/128$ corresponds to the estimated diffusivity one would expect when going from $R/L_T = 9$ to $R/L_T = 11$. Here, the "expected" value is computed by assuming that the ratio $\chi_{(R/L_T=11)}/\chi_{(R/L_T=9)} \approx 1.35$ of reference [36] holds. It is striking to notice that the observed deviation from gyro-Bohm scaling is similar for all three codes. Indeed, the observed transition of GYSELA data, which occurs in between $\rho_* = 1/128$ and $\rho_* = 1/256$, lies far beyond the error bars associated to each point, even when accounting for the discrepancy in the R/L_T values. From another perspective, the typical size of the avalanches as well as the distance between strongly sheared zonal flow layers is typically found to level off below $\rho_* \lesssim 1/256$ [27]. The physics underpinning the saturation of this "staircase" is still unclear.

Consistently, the correlation length λ_c of the electric potential fluctuations exhibits a convincing scaling with ρ_i, independent of the system size, as evident on Fig. 6a. These radial auto-correlation functions are computed on the equatorial plane, at $\theta_0 = 0$ (low field side). It is interesting to notice that the radial correlation length λ_c, defined here as the half width at half maximum of the auto-correlation function of the electric potential fluctuations, varies by almost a factor two from low to high field side of the tokamak, as evident on Fig. 6b: turbulent eddies are more elongated in the unstable low field side region. Such an observation is consistent with the ballooned character of ITG turbulence. The previously reported interaction between zonal flows and avalanches, leading to the limitation of the avalanche size at meso-scales, could provide the explanation as to considering why avalanche dominated regimes still exhibit a gyro-Bohm scaling. Indeed, Bohm scaling of turbulent transport is naturally expected when the correlation length of turbulence depends on the system size (typically for $\lambda_c \sim (a\rho_i)^{1/2}$). Although they are non local in essence, it turns out that avalanches are still limited to intermediate (or meso-) scales, such that they actually do not "feel" the system size.

As far as the correlation time τ_c is concerned, the low time resolution of the saved data leads to significant uncertainties. Table 1 displays the correlation times, estimated from the time lag at which the correlation function cross the abscissa axis. They appear to scale with the effective time a/v_{th}, and more precisely of the order of $\tau_c \sim 2.5\, a/v_{th}$. One point departs from such a value (ORB5 case at $\rho_* = 1/180$). However, the data is not precise enough to allow one to draw a definitive conclusion.

Last but not least, the possibility of triggering transport barriers has been explored. Experimentally, internal transport barriers (ITBs) often develop in the vicinity of low order rational resonant surfaces and weak magnetic shear regions, at least in JET [37]. In this context, GYSELA simulations with hollow and monotonic q profiles have been compared. The hollow-q case exhibits a large radial gap region without any resonant mode across q_{min}. No transport barrier was observed, although different heat source magnitudes and increasing gap widths have been explored [38].

Code	GYSELA		ORB5		
$1/\rho_*$	256	512	140	180	280
$\tau_c\,v_{th}/a$	2.59	2.31	2.57	4.08	2.41
Uncertainty	$2.50 \to 3.12$	$1.87 \to 2.50$	$0 \to 2.86$	$2.86 \to 5.71$	$0 \to 2.83$

Table 1. Auto-correlation time τ_c (3rd row) of the electric potential fluctuations for different ρ_* values. τ_c corresponds to the inversion point of the auto-correlation function, as measured by linear interpolation. The so-called "uncertainty" (4th row) refers to the two neighboring time values for which the auto-correlation function changes sign.

Conversely, turbulent transport dramatically drops (by 2 orders of magnitude) in the gap region when an artificial conical Fourier filter is applied, which only retains resonant modes in the simulation domain. Namely, those modes characterized by $q_{min} \leq -m/n \leq q_{max}$ are kept, where q_{min} and q_{max} are the minimum and maximum values of the safety factor profile, and m and n stand for the poloidal ant toroidal Fourier wave numbers. Such gyrokinetic simulations reconcile – and extend to the turbulence flux-driven regime – previously published contradictory results on the topic. Indeed, a transport barrier was observed in fluid simulations where resonant modes only were accounted for [39], while no barrier was reported in gyrokinetic simulations including all modes [40, 41]. As a matter of fact, the latter simulations pointed out the crucial role of non resonant modes in the low magnetic shear region. Understanding and reproducing the experimental triggering of internal transport barriers still remains an active topic.
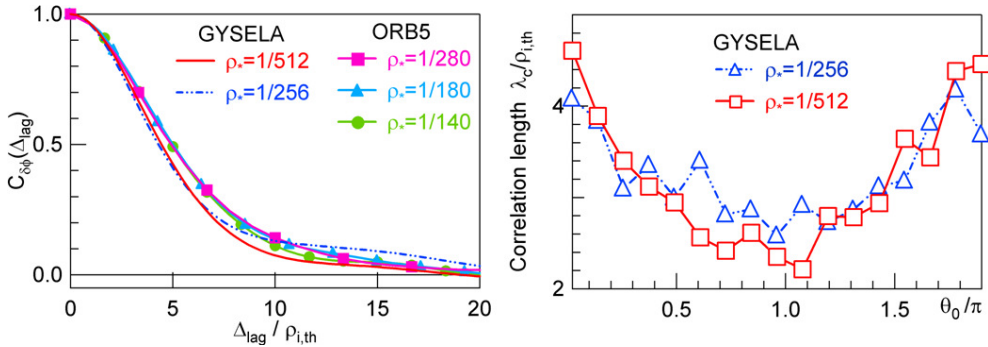

Figure 6. (a) Auto-correlation function of the electric potential fluctuations for different ρ_* values. (b) Normalized radial correlation length (full width half maximum of the auto-correlation function) as a function of the poloidal angle θ_0.

4. Poloidal and toroidal flows

Poloidal rotation is a key player in the dynamics of turbulence eddies [42]. On the one hand, because of the large friction due to trapped particles, it is usually assumed to be governed by the neoclassical theory in tokamak plasmas, i.e. proportional to the equilibrium ion temperature gradient. On the other hand, collisions linearly damp the turbulence self-generated zonal flows. A twofold scan in the turbulence drive and

in collisionality with GYSELA has revealed that turbulence itself can indeed generate a significant amount of poloidal momentum. This tendency is amplified when collisionality decreases, and may therefore be important when considering ITER relevant parameters [43]. Although the magnitude of the turbulence-generated poloidal rotation remains weak with respect to the neoclassical prediction – at least in the absence of any transport barrier – such a turbulence drive modifies the velocity shear, mainly through the turbulent corrugation of the mean profiles. This result can have significant impact on the way experimental data are analyzed, and on experimental predictions regarding turbulence saturation by the mean $\mathbf{E} \times \mathbf{B}$ shearing rate. In order to illustrate this point, let us consider the radial electric field, governed by the radial force balance equation, which is always satisfied within a few percent in GYSELA: $E_r = \nabla_r p_i / en - v_\theta B_\varphi + v_\varphi B_\theta$. At least two means can be used to compute E_r: one can either assume that v_θ is constrained by the neoclassical viscosity, often taken by experimentalists in the absence of direct measurement, or v_θ may be taken from numerical simulations. In this latter case, the total particle poloidal rotation velocity is considered, namely: $n_i v_\theta = \{\langle \dot{\mathbf{x}}_G \rangle_f - \boldsymbol{\nabla} \times \langle \mu \mathbf{b} \rangle_f\} . \mathbf{e}_\theta$, with the notation $\langle ... \rangle_f \equiv \iint \mathcal{J}_v \, d\mu \, dv_{G\parallel} ... f$. The second term in the parenthesis stands for the magnetization velocity [18, 19]. Obviously, only the latter method provides the correct prediction for E_r. The corresponding $\mathbf{E} \times \mathbf{B}$ shearing rates $\gamma_E \approx |\partial_r E_r / B|$, normalized to the maximum linear growth rate γ_{lin}, are plotted on Fig. 7 for both methods. It appears that γ_E would be underestimated almost everywhere if v_θ were assumed neoclassical, meaning once again here that a crucial piece of physics is embedded in the turbulence-induced mean profile dynamics. Also notice that γ_E / γ_{lin} approaches unity at some locations ($\gamma_E / \gamma_{lin} \approx 0.8$ at maximum), suggesting that the system is close to linear stabilization according to linear criteria [42, 44, 45]. Still, such a local analysis looks inappropriate, since global flux-driven systems appear to exhibit time averaged temperature gradients arbitrarily close to the linear stability threshold while exhibiting non vanishing turbulent transport, in contrast with predictions from local approaches [46]. More surprisingly, the instantaneous temperature gradient can explore the stable domain a large fraction of time, as reported in reference [22].
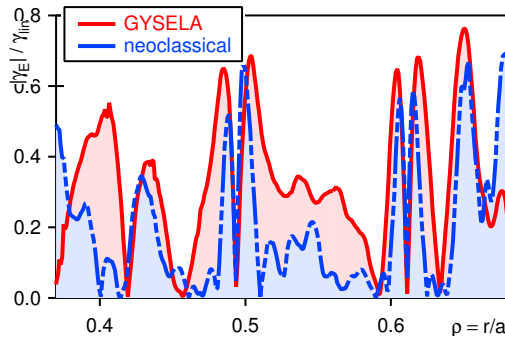

Figure 7. $\mathbf{E} \times \mathbf{B}$ shearing rate normalized by the linear growth rate as a function of the radius. The radial electric field used to compute γ_E derives from the force balance, either by assuming that v_θ is neoclassical, or by taking the actual value of v_θ from the code.

It is interesting to notice that turbulent eddies do not actually rotate at the same

frequency as the ions. Indeed, the linear theory indicates that the real frequency of the fluctuations should be $\omega \approx \omega_E + \omega_n^*$, with $\omega_n^* = (k_\theta \rho_i) v_T \partial_r (\log n)$ the part of the diamagnetic frequency due to the density gradient and $\omega_E = (k_\theta \rho_i) v_T \partial_r \langle \phi \rangle$ the Doppler shift governed by the radial gradient of the mean electric potential. The latter is usually dominant, unless steep density gradients develop. This is consistent with the fact that only the radial shear of $\mathbf{E} \times \mathbf{B}$ flows, and not the shear of the total poloidal plasma flow, plays the critical role of turbulence stabilization. A more detailed analysis reveals that this poloidal flow does not depend critically on the mode number, at least up to $k_\theta \rho_i = 1$. Experimental measurements suggest that, possibly depending on the underlying dominant instability (ITG or trapped electron modes), such a flow actually varies with the mode number, at least for small scales and at sufficiently large collisionality [47]. So far, we have not explored the fluctuation spectra at the largest collisionality reported in reference [47], for which decay of eddy poloidal rotation with $k_\perp$ is observed. We note that, due to the simplified gyro-average operator used in GYSELA, sub-Larmor scales are presently over-damped, preventing us to explore the $k_\theta \rho_i > 1$ region.

Toroidal rotation is another important player in the system dynamics because its shear may reduce the turbulent transport level. Also, it is a critical MHD parameter for it tends to stabilize deleterious modes, the so-called Resistive Wall Modes. However, the amount of injected torque is expected to be very small in ITER. Plasma rotation should then be governed by non linear processes of angular momentum transport and redistribution. From Eq. 1, an exact conservation equation can be derived for the local toroidal angular momentum $\mathcal{L}_\varphi = \sum_s m_s \int d\tau^* u_\varphi f$, where the toroidal component of the velocity is $u_\varphi = (I/B) v_{G\parallel}$ (with $\mathbf{B} = I \boldsymbol{\nabla} \varphi + \boldsymbol{\nabla} \varphi \times \boldsymbol{\nabla} \chi$) and $d\tau^*$ is the elementary reduced phase space volume, excluding the radial direction χ. The equation reads:

$$\partial_t \mathcal{L}_\varphi + \partial_\chi \left(\Pi_\varphi^\chi + \mathrm{T}_\varphi^\chi \right) = \mathsf{J} \tag{6}$$

Here, Π_φ^χ is the $(\varphi \chi)$ off-diagonal component of the Reynolds stress tensor and T_φ^χ the off-diagonal part of the Maxwell stress tensor due to the polarization field [48]. The following definitions hold:

$$\Pi_\varphi^\chi = \sum_s m_s \int d\tau^* \, u_\varphi v_G^\chi f \tag{7}$$

$$\mathrm{T}_\varphi^\chi = \sum_s e_s \int^\chi d\chi \int d\tau^* \, \partial_\varphi \bar{\phi} \, f \tag{8}$$

$$\mathsf{J} = \sum_s e_s \int d\tau^* \, v_G^\chi f \tag{9}$$

We have introduced the radial contravariant component of the velocity $v_G^\chi = \dot{\mathbf{x}}_G \cdot \boldsymbol{\nabla} \chi$. It contains both the $\mathbf{E} \times \mathbf{B}$ and the magnetic drifts, which govern the turbulent and neoclassical contributions, respectively. This equation is reminiscent of the source of spin up proposed in [53]. Provided that the radial current J of gyrocenters is zero, the radial integral of $\mathcal{L}_\varphi$ vanishes, as it should. This constraint is naturally fulfilled by the gyrokinetic equation due to charge conservation, $\partial_t \rho + \partial_\chi \mathsf{J} = 0$, or alternatively after radial integration: $\partial_t \sigma - \mathsf{J} = 0$ (up to a divergence free component of the current, typically a magnetization contribution), where σ is the flux surface integral of the contravariant radial component of the polarization vector ($\partial_\chi \sigma = -\rho$) [9]. It then readily appears that $\mathsf{J} = 0$ in the steady state regime. The comprehensive derivation of this

conservation equation, as well as detailed analysis of numerical results, is presented elsewhere [48]. The same expression Eq. 6 has been obtained in reference [49], and this equation is consistent with the fluid derivation proposed in reference [50]. One can already check on Fig. 8 that the local balance, Eq. 6, is well satisfied in the nonlinear regime. The turbulent and neoclassical contributions are discriminated by considering the radial component of either the electric $\mathbf{E} \times \mathbf{B}$ drift or of the magnetic (both curvature and so-called grad$B$) drifts when computing v_G^χ in eq.7. Also, it appears that the radial current is indeed vanishing, with the main contributions being due to the turbulent and neoclassical stresses.
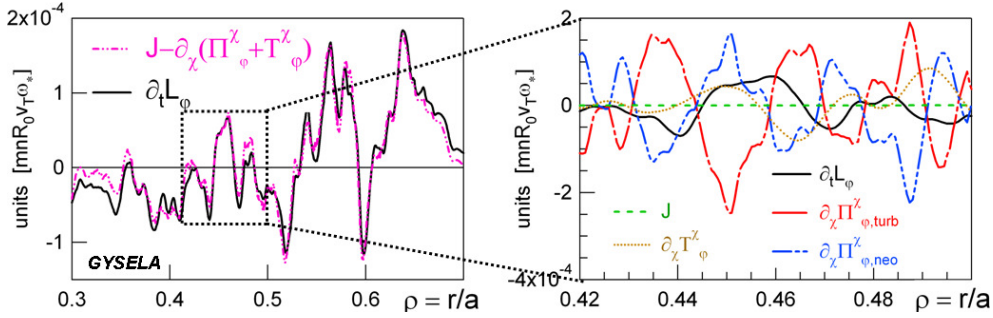
Figure 8. (a) Local balance of toroidal momentum. (b) Detail of various components. Each component is integrated in time. The time window for the integration is $\omega_{c0}\Delta t = 20\,160$, and includes 64 data points.

Here, we wish to highlight some kinetic properties of toroidal flow generation by turbulence. In the simulations run so far, there isn't any prescribed source of toroidal rotation in the system. The outer radial boundary condition is such that u_φ vanishes at r_{max}. Its radial gradient is forced to zero at the inner boundary r_{min}. The outer (close to r_{max}) radial buffer layer, where finite radial diffusion is imposed, then generates a net flow of parallel momentum, which is either positive (outflow) or negative (inflow). In such a case, the magnitude of the toroidal flow does not exceed a few percent of the thermal velocity, as shown in Fig 9. The finite initial value of the parallel flow results from the initial equilibrium distribution function, chosen to be a canonical Maxwellian. The exponential growth of $u_\parallel$, starting at $\omega_{c0}t \approx 3.10^4$, is then characteristic of the linear regime of the instability. Finally, the last part corresponds to the saturated turbulence regime. We note that the flux surface average of u_φ remains co-current, this is consistent with many experimental observations in tokamaks [51, 52]. Figure 10a shows, in velocity space $v_\perp - v_{G\parallel}$, the quantity $I_{v_\parallel} = v_\perp v_{G\parallel} \langle f(\mathbf{x}_0, v_\perp, v_{G\parallel}, t) - f(\mathbf{x}_0, v_\perp, -v_{G\parallel}, t) \rangle$, with $\mathbf{x}_0 = (\rho = 0.5, \theta = 0, \varphi = 0)$. The average is performed in time during the non linear phase, from $\omega_{c0}t = 5.10^4$ to 9.10^4. The integral $\int_0^{+\infty} \int_0^{+\infty} I_{v_\parallel} \, \mathrm{d}v_\perp \, \mathrm{d}v_{G\parallel}$ is proportional to the local toroidal flow, at the position $\mathbf{x}_0$. The oblique line refers to the trapped-passing boundary $v_\perp = \sqrt{2\epsilon} v_{G\parallel}$ (with $\epsilon = r/R_0$). The plain circular line, which corresponds to $I_{v_\parallel} = 0$, turns out to coincide with the thermal energy $m_i({v_{G\parallel}}^2 + v_\perp^2)/2 = 3T/2$. $I_{v_\parallel}$ is extremal close to the trapped/passing boundary: maximal (positive) for $v \equiv (v_\perp^2 + {v_{G\parallel}}^2)^{1/2} \approx 2.5 v_T$, minimal (negative) near $v \simeq 1.3 v_T$, and almost vanishing elsewhere. It follows that the toroidal flow is carried out by supra-thermal barely passing particles. Interestingly

enough, similar phase space structures of the turbulence driven toroidal flux are also reported in ITG driven turbulence with the GTS code (see Fig.16 of reference [54]). In addition, it is worth comparing this kinetic structure with the quasi-linear expression of the radial flux of toroidal momentum Γ_{v_φ}. Neglecting the radial variation of the toroidal flow – which is legitimate given the small magnitude of V_φ – and of the density profile – which is rather flat in these simulations –, and further assuming similar transverse and parallel temperatures, $\Gamma_{v_\varphi}^{QL}$ is proportional to $I_{v_\parallel}^{QL}$, in the sense that $\Gamma_{v_\varphi} \propto \int_0^{+\infty} dv_\perp \int_{-\infty}^{+\infty} dv_{G\parallel} I_{v_\parallel}^{QL}$:

$$I_{v_\parallel}^{QL} = v_\perp \left(\frac{E}{T} - \frac{3}{2} \right) \left(3m_i v_{G\parallel}^2 + \frac{1}{2} m_i v_\perp^2 \right) e^{-E/T} \tag{10}$$

with $E = m_i(v_{G\parallel}^2 + v_\perp^2)/2$. The detailed derivation has been proposed by several authors [55, 56, 57]. Here, we propose a simplified derivation by considering the following linearized gyrokinetic equation for the perturbed distribution function δf, obtained when neglecting the parallel dynamics: $(\partial_t + \mathbf{v}_D.\boldsymbol{\nabla})\delta f = -v_{Er}\partial_r f_{eq}$, with $\mathbf{v}_D$ and $\mathbf{v}_E$ the curvature and grad-B drift and the electric drift, respectively. Here, the equilibrium distribution function is taken Maxwellian: $f_{eq} = n(2\pi T/m)^{-3/2} \exp\{-(mu_{G\parallel}^2/2 + \mu B)/T\}$, with $u_{G\parallel} = v_{G\parallel} - V_\parallel$ the velocity in the co-moving frame. Then, using Fourier decomposition, the quasi-linear expression of the radial flux of parallel momentum $\Gamma_{V_\parallel} \equiv \langle \int (2\pi/m)B \, d\mu \, dv_{G\parallel} \, v_{Er} m v_{G\parallel} f \rangle$ can be recast as follows: $\Gamma_{V_\parallel}^{QL} = \Im \sum_{k,\omega} \int 2\pi B \, d\mu \, dv_{G\parallel} |\hat{v}_{Ek}|^2 f_{eq} \hat{I}_{k,\omega}$, where $\hat{I}_{k,\omega} = v_{G\parallel}\partial_r(\log f_{eq})/(\omega + i\Delta\omega + \omega_D)$ and $\omega_D = (mv_{G\parallel}^2 + \mu B)/eB \, \mathbf{k}.(\mathbf{b} \times \boldsymbol{\nabla} \log B)$. Here, $\Delta\omega$ accounts for turbulence broadening effects. In the hydrodynamic limit $(\omega + i\Delta\omega) \gg \omega_D$, and keeping only even terms in $u_{G\parallel}$ due to symmetry properties of the integrand, expression eq. 10 can then be recovered. $I_{v_\parallel}^{QL}$ is displayed on Fig. 10b. Keeping in mind that we have retained a simplified expression for $\Gamma_{v_\varphi}^{QL}$, and that $I_{v_\parallel}$ is not flux surface averaged, the qualitative agreement between both quantities is remarkable.
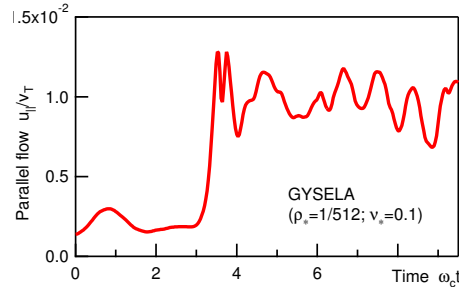

Figure 9. Time evolution of the flux surface averaged toroidal flow at mid-radius in GYSELA.

5. Discussion and conclusions

This paper reports on global gyrokinetic simulations of ITG turbulence in the flux-driven regime with the three codes GYSELA, ORB5 and XGC1. Three main conclusions can be drawn. First of all, the transport dynamics is largely dominated
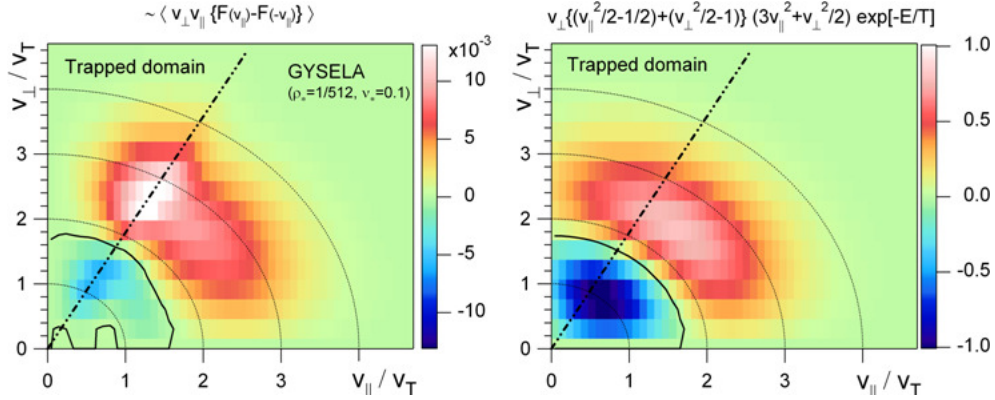
Figure 10. Structure in velocity space (a) of the integrand $I_{v_\parallel}$ leading to the fluid toroidal flow, and (b) of the integrand $I_{v_\parallel}^{QL}$ governing the quasi-linear expression of the radial flux of toroidal momentum (see text).

by avalanches, of characteristic radial velocity $\rho_* v_T$. Although they can propagate radially on much larger radial distances than the Eulerian correlation length of turbulent eddies, the effective heat diffusivity still exhibits a gyro-Bohm scaling, at least when $\rho_* \approx 1/300$. The proposed explanation for such a surprising result comes from the fact that zonal flows, which efficiently contribute to turbulence saturation, appear to remain meso-scale: they exhibit a wave-like radial structure, with a characteristic wave-length almost independent of the system size. Secondly, turbulence is found to generates small amplitude – with respect to the neoclassical prediction $v_{\theta,neo}$ – poloidal mean flow, which however significantly modifies the corrugation of $v_{\theta,neo}$ radial profile. This trend increases when collisionality decreases. As a result, it turns out that computing the radial electric field from the force balance, with the assumption that v_θ is given by the neoclassical theory, can lead to significant underestimations (by factors) of the resulting $\mathbf{E} \times \mathbf{B}$ shearing rate. Such hypothesis, which is often adopted when analyzing experimental data, can reveal particularly misleading when studying the possible stabilization of turbulence, at least at small collisionality. Finally, intrinsic toroidal rotation appears to be mainly driven by the turbulent and neoclassical stresses, when any net radial polarization current is inhibited by the adiabatic electron model. Furthermore, such an intrinsic toroidal flow, of the order of a few percent of the thermal velocity, appears to be mainly carried by barely passing supra-thermal particles, in fair agreement with quasi-linear predictions.

Acknowledgments

Appendix A. Source terms in GYSELA

This appendix comprehensively details the expression and properties of the various source terms in GYSELA. Especially, it allows the reader to understand the reason for such a specific expression of the heat source in GYSELA (see eq. 4), as resulting from the constraint of independency of momentum, heat and polarization sources. Focussing on the source term, the gyrokinetic equation reads, in normalized units:

$$\frac{\mathrm{d}\hat{f}}{\mathrm{d}\hat{t}} = \hat{S}_E(\hat{r}, \hat{\theta}, \hat{v}_\parallel, \hat{\mu})\hat{S}_r(\rho) \tag{A.1}$$

where $\rho = \hat{r}/\hat{L}_r = \lambda^{-1}\rho_*\hat{r}$. Here, λ represents the fraction of the minor radius which is considered: $\hat{L}_r = \hat{r}_{max} - \hat{r}_{min} = \lambda/\rho_*$, with $0 < \lambda \leq 1$ and $\rho_* = \rho_0/a = 1/\hat{a}$. The energy dependent part of the source is decomposed on the basis of orthogonal Hermite and Laguerre poynomials (cf. section Appendix A.4):

$$\hat{S}_E(\hat{r}, \hat{\theta}, \hat{v}_\parallel, \hat{\mu}) = \sum_{\ell=0}^{+\infty}\sum_{h=0}^{+\infty} c_{h\ell}H_h(\bar{v}_{G\parallel})L_\ell(\bar{\mu})e^{-\bar{v}_{G\parallel}^2-\bar{\mu}} \tag{A.2}$$

where the $c_{h\ell}$ coefficients depend on the space coordinates only. The following definitions have been introduced:

$$\bar{\mu} \equiv \frac{\hat{\mu}\hat{B}}{\hat{T}_s} \qquad ; \qquad \bar{v}_{G\parallel} \equiv \frac{\hat{v}_\parallel}{\sqrt{2\hat{T}_s}} \tag{A.3}$$

with $\hat{T}_s$ the normalized source temperature.

Appendix A.1. Corresponding sources for fluid moments

Let's derive the corresponding source of matter $\hat{\mathbb{S}}_n$, of parallel momentum $\hat{\mathbb{S}}_{v_{G\parallel}}$, of energy $\hat{\mathbb{S}}_\mathcal{E}$ and of vorticity $\hat{\mathbb{S}}_\Omega$. With the adopted definitions, $\hat{B}_\parallel^* = \hat{B}(1+\hat{J}_{\parallel B}\bar{v}_{G\parallel})$ and $\hat{J}_{\parallel B} \equiv \sqrt{2\hat{T}_s}\,\hat{J}_\parallel/\hat{B}^2$. The parallel current $\hat{J}_\parallel = \vec{b}.\hat{\vec{J}}$ is prescribed in GYSELA. Then, the integral over the velocity space reads as follows:

$$\int \mathrm{d}^3\vec{v} \equiv \int_{-\infty}^{+\infty} \mathrm{d}\hat{v}_\parallel \int_0^{+\infty} 2\pi\hat{B}_\parallel^* \,\mathrm{d}\hat{\mu} = \frac{(2\pi\hat{T}_s)^{3/2}}{\sqrt{\pi}}\int_{-\infty}^{+\infty}(1+\hat{J}_{\parallel B}\bar{v}_{G\parallel})\,\mathrm{d}\bar{v}_{G\parallel}\int_0^{+\infty}\mathrm{d}\bar{\mu}$$

Notice that $(1 + \hat{J}_{\parallel B}\bar{v}_{G\parallel}) = H_0 + \frac{\hat{J}_{\parallel B}}{2}H_1(\bar{v}_{G\parallel})$.

The fluid source of matter $\hat{\mathbb{S}}_n$ is simply $\hat{\mathbb{S}}_n \equiv \int \mathrm{d}^3\vec{v}\,\hat{S}_E\hat{S}_r$. Using the decomposition of S_E on the basis of orthogonal polynomials eq. A.2, the source of matter becomes:

$$\hat{\mathbb{S}}_n = (2\pi\hat{T}_s)^{3/2}\left(c_{00} + \hat{J}_{\parallel B}\,c_{10}\right)\hat{S}_r \tag{A.4}$$

The fluid source of parallel momentum $\hat{\mathbb{S}}_{v_{G\parallel}}$ reads as follows: $\hat{\mathbb{S}}_{v_{G\parallel}} \equiv \int \mathrm{d}^3\vec{v}\, \hat{v}_\parallel \hat{S}_E \hat{S}_r$. Following the same procedure than for the density source, one finally obtains:

$$\hat{\mathbb{S}}_{v_{G\parallel}} = 2\pi^{3/2}\hat{T}_s^2 \left[2c_{10} + \hat{J}_{\parallel B}(c_{00} + 4c_{20})\right] \hat{S}_r \tag{A.5}$$

The fluid source of energy $\hat{\mathbb{S}}_{\mathcal{E}}$ is defined as follows: $\hat{\mathbb{S}}_{\mathcal{E}} \equiv \int \mathrm{d}^3\vec{v} \left(\frac{\hat{v}_\parallel^2}{2} + \hat{\mu}\hat{B}\right) \hat{S}_E \hat{S}_r$. Notice that $(\hat{v}_\parallel^2/2 + \hat{\mu}\hat{B}) = \hat{T}_s(\bar{v}_{G\parallel}^2 + \bar{\mu}\hat{B})$. Again, the energy source can be recast in terms of the $c_{h\ell}$ coefficients:

$$\hat{\mathbb{S}}_{\mathcal{E}} = (2\pi)^{3/2}\hat{T}_s^{5/2} \left[2\,c_{20} + \frac{3}{2}\,c_{00} - c_{01} \right.$$
$$\left. + \frac{5}{2}\hat{J}_{\parallel B}\,c_{10} + 6\hat{J}_{\parallel B}\,c_{30} - \hat{J}_{\parallel B}\,c_{11}\right] \hat{S}_r \tag{A.6}$$

The fluid source of vorticity $\hat{\mathbb{S}}_\Omega$ is simply: $\hat{\mathbb{S}}_\Omega \equiv \int \mathrm{d}^3\vec{v}\, J_0.(\hat{S}_E \hat{S}_r)$, where J_0 is the gyro-average operator. We use the Padé approximation:

$$J_0 \approx 1 + \frac{\hat{\mu}}{2\hat{B}}\nabla_\perp^2 = 1 + \frac{\hat{T}_s}{2\hat{B}^2}\,\bar{\mu}\nabla_\perp^2$$

Again, the vorticity source can be recast in terms of the $c_{h\ell}$ coefficients:

$$\hat{\mathbb{S}}_\Omega = \hat{\mathbb{S}}_n + (2\pi\hat{T}_s)^{3/2} \left[\frac{\hat{T}_s}{2}\,\nabla_\perp^2 \left(\frac{(c_{00} - c_{01})\hat{S}_r}{\hat{B}^2}\right) \right.$$
$$\left. + \hat{J}_{\parallel B}\frac{\hat{T}_s}{2}\,\nabla_\perp^2 \left(\frac{(c_{10} - c_{11})\hat{S}_r}{\hat{B}^2}\right)\right] \tag{A.7}$$

Appendix A.2. Pure sources of momentum, energy and vorticity

The expressions of $\hat{\mathbb{S}}_n$ (eq. A.4), $\hat{\mathbb{S}}_{v_{G\parallel}}$ (eq. A.5), $\hat{\mathbb{S}}_{\mathcal{E}}$ (eq. A.6) and $\hat{\mathbb{S}}_\Omega$ (eq. A.7) provide the constraints on the $c_{h\ell}$ coefficients in order to impose independently zero source of density, of momentum, of energy or of vorticity. Let's consider three cases:

- Non vanishing source of energy, with no injection of particles nor of momentum.
- Non vanishing source of momentum, with no injection of particles nor of energy.
- Non vanishing source of vorticity, with no injection of particles, of momentum nor of energy.

These three cases are considered hereafter. Imposing zero source of matter, which is mandatory in the present version of GYSELA with adiabatic electrons, leads to the following constraint:

$$\hat{\mathbb{S}}_n = 0 \quad \Rightarrow \quad c_{00} + \hat{J}_{\parallel B}\,c_{10} = 0 \tag{A.8}$$

Also, the fluid sources of parallel momentum, of energy and of vorticity are proportional to:

$$\hat{\mathbb{S}}_{v_\parallel} \propto \left(2 - \hat{J}_{\parallel B}^2\right)\,c_{10} + 4\hat{J}_{\parallel B}\,c_{20} \tag{A.9}$$

$$\hat{\mathbb{S}}_{\mathcal{E}} \propto 2c_{20} - c_{00} + 6\hat{J}_{\parallel B}\,c_{30} - \left(c_{01} + \hat{J}_{\parallel B}\,c_{11}\right) \tag{A.10}$$

$$\hat{\mathbb{S}}_\Omega \propto -\nabla_\perp^2 \left(\frac{\hat{J}_{\|B} c_{10} \hat{S}_r}{\hat{B}^2} \right) + \hat{J}_{\|B} \nabla_\perp^2 \left(\frac{c_{10} \hat{S}_r}{\hat{B}^2} \right)$$

$$-\nabla_\perp^2 \left(\frac{c_{01} \hat{S}_r}{\hat{B}^2} \right) - \hat{J}_{\|B} \nabla_\perp^2 \left(\frac{c_{11} \hat{S}_r}{\hat{B}^2} \right) \tag{A.11}$$

Appendix A.2.1. *Pure source of energy* Killing the fluid sources of particles, momentum and vorticity, while keeping finite the fluid source of energy, imposes eq. A.9 and eq. A.11 to vanish. Several solutions can be envisaged. Let's choose $c_{30} = 0$ and $(c_{01} + \hat{J}_{\|B} c_{11}) = 0$, with $(2c_{20} - c_{00}) \neq 0$. Then, the fluid source of vorticitiy trivially vanishes for $c_{10} = c_{11}$. To summarize, we propose the following set of coefficients for a pure source of energy:

$$\begin{cases} c_{11} = c_{10} = -\frac{4\hat{J}_{\|B}}{2 - \hat{J}_{\|B}^2} c_{20} \\ c_{00} = c_{01} = \frac{4\hat{J}_{\|B}}{2 - \hat{J}_{\|B}^2} c_{20} \end{cases}$$

with $c_{20} \neq 0$.

In order to inject solely energy into the system, the source term that should appear in the right hand side of the gyrokinetic equation would then take the following form:

$$\hat{S}_E^{\mathcal{E}} = \frac{\hat{S}_0^{\mathcal{E}} \hat{S}_r}{\sqrt{2}\pi^{3/2}\hat{T}_s^{5/2}} \left[\bar{v}_{G\|}^2 - \frac{1}{2} \right.$$

$$\left. -\frac{\hat{J}_{\|B}}{2 - \hat{J}_{\|B}^2} (2 - \bar{\mu}) \left(2\bar{v}_{G\|} - \hat{J}_{\|B} \right) \right] e^{-\bar{v}_{G\|}^2 - \bar{\mu}} \tag{A.12}$$

where we have introduced the normalized intensity: $\hat{S}_0^{\mathcal{E}} \equiv [2(2\pi)^{3/2}\hat{T}_s^{5/2}]\, c_{20}$. The fluid source of energy would have the following magnitude:

$$\hat{\mathbb{S}}_{\mathcal{E}} = \left(1 - \frac{4\hat{J}_{\|B}^2}{2 - \hat{J}_{\|B}^2} \right) \hat{S}_0^{\mathcal{E}} \hat{S}_r \tag{A.13}$$

Then, up to small terms proportional to $\hat{J}_{\|B}$, $\hat{S}_r$ provides the radial shape of the energy source, while $\hat{S}_0^{\mathcal{E}}$ gives its magnitude (Provided $\hat{S}_r$ is properly normalized, i.e. such that its volume integral is equal to unity).

Appendix A.2.2. *Pure parallel momentum* Killing the fluid sources of particles, energy and vorticity, while keeping finite the fluid source of parallel momentum, imposes eqs. A.10-A.11 to vanish. Again, several options could be considered. We follow the same strategy as for the energy, namely:

$$\begin{cases} c_{11} = c_{10} \\ c_{00} = c_{01} = -\hat{J}_{\|B}\, c_{10} \end{cases}$$

Then, the source of energy vanishes if $c_{30} = 0$ and $2\, c_{20} = c_{00}$.

Consistently, in order to inject only parallel momentum, the following source is proposed:

$$\hat{S}_{v_\parallel} = \frac{\hat{S}_0^{v_\parallel} \hat{S}_r}{4\pi^{3/2}\hat{T}_s^2} \left[2\bar{v}_{G\parallel}(2-\bar{\mu}) \right.$$
$$\left. -\hat{J}_{\parallel B}\left(1 + 2\bar{v}_{G\parallel}^2 - \bar{\mu}\right)\right] e^{-\bar{v}_{G\parallel}^2 - \bar{\mu}} \tag{A.14}$$

The corresponding fluid source of momentum is:

$$\hat{\mathbb{S}}_{v_\parallel} = \left(1 - \frac{3\hat{J}_{\parallel B}}{2}\right) \hat{S}_0^{v_\parallel} \hat{S}_r \tag{A.15}$$

Then, at leading order in $\hat{J}_{\parallel B}$, $\hat{S}_r$ corresponds to the radial shape of the momentum source, and $\hat{S}_0^{v_\parallel}$ to its magnitude.

Appendix A.2.3. Pure source of vorticity So as to inject vorticity only, the simplest choice appears to be: $c_{00} = c_{10} = c_{11} = 0$ and $c_{20} = 0$. Then the source of vorticitiy is governed by the c_{01} coefficient only: $\hat{\mathbb{S}}_\Omega \propto -\nabla_\perp^2(c_{01}\hat{S}_r)$, while that of momentum eq. A.9 is set to zero. The source of energy eq. A.10 vanishes provided that $c_{30} = (\hat{B}/6\hat{J}_{\parallel B})\,c_{01}$. Obviously, such a constraint is invalid for those simulations performed at vanishing parallel current.

Alternatively, we have decided to allow for some parallel momentum injection by taking $c_{20} = \hat{B}\,c_{01}/2 \neq 0$ and $c_{30} = 0$. Then, the source term to be considered is the following:

$$\hat{S}_\Omega = \frac{\hat{S}_0^\Omega \hat{S}_r}{\sqrt{2}\,\pi^{3/2}\hat{T}_s^{5/2}} \left[1 - \bar{\mu} + \left(2\bar{v}_{G\parallel}^2 - 1\right)\right] e^{-\bar{v}_{G\parallel}^2 - \bar{\mu}} \tag{A.16}$$

The resulting fluid source of vorticity is:

$$\hat{\mathbb{S}}_\Omega = \nabla_\perp^2 \left(\frac{\hat{S}_r}{\hat{B}^2}\right) \tag{A.17}$$

We recall that such a source does inject some momentum as well. However, its magnitude remains small, and equal to $(-4\hat{J}_\parallel\,\hat{S}_0^\Omega\hat{S}_r)$.

Appendix A.3. Summary

To summarize, the following general expression is retained for the kinetic source:

$$\frac{\mathrm{d}\hat{f}}{\mathrm{d}\hat{t}} = \left\{ \left[\bar{v}_{G\parallel}^2 - \frac{1}{2} - \frac{\hat{J}_{\parallel B}}{2 - \hat{J}_{\parallel B}^2}\,(2-\bar{\mu})\left(2\bar{v}_{G\parallel} - \hat{J}_{\parallel B}\right)\right]\frac{\hat{S}_0^{\mathcal{E}}}{2(2\pi)^{3/2}\hat{T}_s^{5/2}}\,\hat{S}_r^{\mathcal{E}} \right.$$
$$+ \left[2\bar{v}_{G\parallel}(2-\bar{\mu}) - \hat{J}_{\parallel B}\left(1 + 2\bar{v}_{G\parallel}^2 - \bar{\mu}\right)\right]\frac{\hat{S}_0^{v_\parallel}}{4\pi^{3/2}\hat{T}_s^2}\,\hat{S}_r^{v_\parallel}$$
$$\left. + \left[1 - \bar{\mu} + \left(2\bar{v}_{G\parallel}^2 - 1\right)\right]\frac{\hat{S}_0^\Omega}{\sqrt{2}\,\pi^{3/2}\hat{T}_s^{5/2}}\,\hat{S}_r^\Omega \right\} e^{-\bar{v}_{G\parallel}^2 - \bar{\mu}} \tag{A.18}$$

with $\bar{\mu} = \hat{\mu}\hat{B}/\hat{T}_s$, $\bar{v}_{G\parallel} = \hat{v}_\parallel/\sqrt{2\hat{T}_s}$ and $\hat{J}_{\parallel B} \equiv \sqrt{2\hat{T}_s}\,\hat{J}_\parallel/\hat{B}^2$.

Appendix A.4. Basic properties of Laguerre and Hermite polynomials

The Hermite and Laguerre polynomials form the set of orthogonal basis with respect to the following scalar products:

$$\text{Laguerre } L_\ell(x) : \int_0^{+\infty} L_\ell L_{\ell'} \mathrm{e}^{-x} \, \mathrm{d}x = \delta_{\ell\ell'} |L_\ell|^2 \tag{A.19}$$

$$\text{Hermite } H_h(x) : \int_{-\infty}^{+\infty} H_h H_{h'} \mathrm{e}^{-x^2} \, \mathrm{d}x = \delta_{hh'} |H_h|^2 \tag{A.20}$$

The Laguerre polynomials are normalized: $|L_\ell|^2 = 1$. The norm of the Hermite polynomials is:

$$|H_h|^2 \equiv \int_{-\infty}^{+\infty} H_h^2 \, \mathrm{e}^{-x^2} \, \mathrm{d}x = \sqrt{\pi} \, 2^h h! \tag{A.21}$$

The five first Laguerre and Hermite polynomials are:

$$\begin{aligned} L_0(x) &= 1 \\ L_1(x) &= 1 - x \\ L_2(x) &= \tfrac{1}{2}(2 - 4x + x^2) \\ L_3(x) &= \tfrac{1}{6}(6 - 18x + 9x^2 - x^3) \\ L_4(x) &= \tfrac{1}{24}(24 - 96x + 72x^2 - 16x^3 + x^4) \end{aligned} \tag{A.22}$$

and

$$\begin{aligned} H_0(x) &= 1 & &\rightarrow & |H_0|^2 &= \sqrt{\pi} \\ H_1(x) &= 2x & &\rightarrow & |H_1|^2 &= 2\sqrt{\pi} \\ H_2(x) &= -2 + 4x^2 & &\rightarrow & |H_2|^2 &= 8\sqrt{\pi} \\ H_3(x) &= -12x + 8x^3 & &\rightarrow & |H_3|^2 &= 48\sqrt{\pi} \\ H_4(x) &= 12 - 48x^2 + 16x^4 & &\rightarrow & |H_4|^2 &= 384\sqrt{\pi} \end{aligned} \tag{A.23}$$

References

[1] Garbet X, Idomura Y, Villard L and Watanabe T H, 2010 *Nucl. Fusion* **50**, 043002
[2] Grandgirard V, Sarazin Y *et al*, 2007 *Plasma Phys. Control. Fusion* **49**, B173
[3] Jolliet S, Bottino A *et al*, 2007 *Comp. Phys. Communications* **177**, 409
[4] Chang C S and Ku S, 2008 *Phys. Plasmas* **15**, 062510; Chang C S *et al*, 2009 *Phys. Plasmas* **16**, 056108
[5] Villard L, Bottino A *et al*, 2010 *Plasma Phys. Control. Fusion* **52**, 124038
[6] Darmet G, Ghendrih Ph, Sarazin Y, Garbet X, Grandgirard V, 2008 *Communications in Nonlinear Science and Numerical Simulation* **13**, 53
[7] Candy J, Holland C, Waltz R E, Fahey M R and Belli E, 2009 *Phys. Plasmas* **16**, 060704
[8] Barnes M, Abel I G, Dorland W, Görler T, Hammett G W and Jenko F, 2010 *Phys. Plasmas* **17**, 056109
[9] Brizard A J and Hahm T S, 2007 *Rev. Mod. Phys.* **79**, 421
[10] Grandgirard V, Brunetti M *et al*, 2006 *J. Comput. Phys.* **217**, 395
[11] Rosenbluth M N and Hinton F L, 1998 *Phys. Rev. Lett.* **80**, 724
[12] Catto P J and Tsang K T, 1977 *Phys. Fluids* **20**, 396
[13] Xu X Q and Rosenbluth M N, 1991 *Phys. Fluids B* **3**, 627
[14] Ku S, Chang C S and Diamond P H, 2009 *Nucl. Fusion* **49**, 115021
[15] Wang W X, Nakajima N, Okamoto M and Murakami S, 1999 *Plasma Phys. Control. Fusion* **41**, 1091
[16] Lin Z, Tang W M and Lee W W, 1995 *Phys. Plasmas* **2**, 2975
[17] Garbet X, Dif-Pradalier G *et al*, 2009 *Phys. Plasmas* **16**, 062503
[18] Dif-Pradalier G, Grandgirard V, Sarazin Y, Garbet X, Ghendrih Ph, *Comm. Nonlinear Science Num. Simul.* **13** (2008) 6571

[19] Dif-Pradalier G, Diamond P H, Grandgirard V *et al*, *Phys. Plasmas* **18** (2011) 062309
[20] Vernay T, Brunner S, Villard L *et al*, 2010 *Phys. Plasmas* **17**, 122301 (2010)
[21] Falchetto G L, Scott B D, Angelino P *et al* 2008 *Plasma Phys. Control. Fusion* **50**, 124015
[22] Sarazin Y, Grandgirard V *et al*, 2010 *Nucl. Fusion* **50**, 054004
[23] McMillan B F, Jolliet S *et al*, 2008 *Phys. Plasmas* **15**, 052308
[24] Garbet X, Sarazin Y *et al*, 1999 *Nucl. Fusion* **39**, 2063
[25] Beyer P, Benkadda S, Garbet X and Diamond P H, 2000 *Phys. Rev. Lett.* **85**, 4892
[26] Sarazin Y, Bécoulet M *et al*, 2002 *Plasma Phys. Control. Fusion* **44** 2445
[27] Dif-Pradalier G, Diamond P H *et al*, 2010 *Phys. Rev. E* **82**, 025401(R)
[28] McMillan B F, Jolliet S *et al*, 2009 *Phys. Plasmas* **16**, 022310
[29] Idomura Y, Urano H, Aiba N and Tokuda S, 2009 *Nucl. Fusion* **49**, 065029
[30] Diamond P H, Itoh S-I *et al*, 2005 *Plasma Phys. Control. Fusion* **47**, R35-R161
[31] Dif-Pradalier G, Diamond P H *et al*, 2011 *Dynamic self-organisation in tokamaks: impact on poloidal rotation, flow shear, heat transport and marginal stability*, in preparation
[32] Villard L, Allfrey S, Bottino A *et al*, 2004 *Nucl. Fusion* **44**, 172
[33] ITER Physics Expert Groups on Confinement and Transport and Confinement Modelling and Database *et al.*, "ITER Physics Basis, Chapter 2", 1999 *Nucl. Fusion* **39**, 2175
[34] McMillan B F, Lapillonne X, Brunner S, Villard L, Jolliet S, Bottino A, Görler T and Jenko F, 2010 *Phys. Rev. Lett.* **105**, 155001
[35] Lapillonne X 2010, PhD thesis 4684, *Local and global Eulerian gyrokinetic simulations of microturbulence in realistic geometry with applications to the TCV Tokamak*, EPFL, http://library.epfl.ch/theses/?nr=4684; Görler T 2009 Ph.D. thesis, Univ. Ulm
[36] Dimits A M, Bateman G, Beer M A *et al*, 2000 *Phys. Plasmas* **7**, 969
[37] Challis C D *et al*, 2002 *Plasma Phys. Control. Fusion* **44**, 1031; Joffrin E, Challis C D *et al*, 2003 *Nucl. Fusion* **43**, 1167
[38] Sarazin Y, Strugarek A *et al*, 2010 *J. Phys. Conf. Series* **260** 012017
[39] Garbet X, Bourdelle C, Hoang G T *et al*, 2001 *Phys. Plasmas* **8**, 2793
[40] Candy J, Waltz R E and Rosenbluth M N, 2004 *Phys. Plasmas* **11**, 1879
[41] Waltz R E, Austin M E, Burrell K H and Candy J, 2006 *Phys. Plasmas* **13**, 052301
[42] Biglari H, Diamond P H and Terry P, 1990 *Phys. Fluids* B **2**, 1
[43] Dif-Pradalier G, Grandgirard V *et al*, 2009 *Phys. Rev. Lett.* **103**, 065002
[44] Hahm T S and Burrell K H, 1995 *Phys. Plasmas* **2**, 1648
[45] Waltz R E, Kerbel G D, Milovich J and Hammett G W, 1995 *Phys. Plasmas* **2**, 2408
[46] Dif-Pradalier G, Diamond P H *et al*, 2011 *Modeling choices in numerical simulations: where do we stand in term of the physics?*, in preparation
[47] Vermare L, Hennequin P, Grcan Ö D, Bourdelle C, Clairet F, Garbet X, Sabot R and the Tore Supra Team, 2011 *Phys. Plasmas* **18**, 012306
[48] Abiteboul J, Garbet X, Grandgirard V *et al* 2011, *Phys. Plasmas* **18**, 082503
[49] Scott B D and Smirnov J, 2010 *Phys. Plasmas* **17**, 112302
[50] Brizard A J, 2010 *Phys. Plasmas* **17**, 112503
[51] Eriksson L-G, Righi E and Zastrow K D, 1997 *Plasma Phys. Control. Fusion* **17**, 27
[52] Rice J E, Bonoli P T, Goetz J A *et al.*, 1999 *Nucl. Fusion* **39**, 1175; Rice J E, Ince-Cushman A, deGrassie J S *et al.*, 2007 *Nucl. Fusion* **47**, 1628
[53] McDevitt C J, Diamond P H *et al*, 2009 *Phys. Rev. Lett.* **103**, 205003
[54] Wang W X, Diamond P H, Hahm T S *et al* 2010 *Phys. Plasmas* **17**, 072511
[55] Hahm T S, Diamond P H, Gürcan Ö D and Rewoldt G, 2008 *Phys. Plasmas* **15**, 055902
[56] Peeters A G, Strintzi D, Camenen Y, Angioni C, Casson F J, Hornsby W A and Snodin A P, 2009 *Phys. Plasmas* **16**, 042310
[57] Garbet X 2009, CEA-IRFM Cadarache, France, 5th *Festival de Théorie* (Aix-en-Provence, France), private communication